

# Few-atom-layer metallene quantum dots as a new paradigm toward ampere-level CO<sub>2</sub> electroreduction to liquid product

**Min Zhang**

Fujian Institute of Research on the Structure of Matter (FJIRSM), Chinese Academy of Sciences (CAS)

**Shenghua Zhou**

Fujian Institute of Research on the Structure of Matter (FJIRSM), Chinese Academy of Sciences (CAS)

**Wenbo Wei**

Fujian Institute of Research on the Structure of Matter (FJIRSM), Chinese Academy of Sciences (CAS)

**Dong-Dong Ma**

Fujian Institute of Research on the Structure of Matter (FJIRSM), Chinese Academy of Sciences (CAS)

**Shu-Guo Han**

Fujian Institute of Research on the Structure of Matter (FJIRSM), Chinese Academy of Sciences (CAS)

**Xiaofang Li**

Fujian Institute of Research on the Structure of Matter (FJIRSM), Chinese Academy of Sciences (CAS)

**Xin-Tao Wu**

Fujian Institute of Research on the Structure of Matter

**Qiang Xu**

SUSTECH

**Qi-Long Zhu** (✉ [qlzhu@fjirsm.ac.cn](mailto:qlzhu@fjirsm.ac.cn))

Fujian Institute of Research on the Structure of Matter (FJIRSM), Chinese Academy of Sciences (CAS) <https://orcid.org/0000-0001-9956-8517>

---

## Article

**Keywords:**

**Posted Date:** April 6th, 2022

**DOI:** <https://doi.org/10.21203/rs.3.rs-1506034/v1>

**License:**  This work is licensed under a Creative Commons Attribution 4.0 International License. [Read Full License](#)

---

## Abstract

Electrocatalytic CO<sub>2</sub> reduction reaction (CO<sub>2</sub>RR) toward commodity chemicals and fuels powered by the renewable electricity presents an enticing prospect, in which the emerging metallenes as catalysts have aroused great interest. Herein, we firstly report the synthesis of a kind of tiny metallene quantum dots (QDs), stanene QDs (Sn-ene QDs), with a few-atom-layer feature and rich edge centers via a fast electrochemical self-reconstruction from the easily-scalable monolayer SnFe-based Prussian blue analogue nanosheets. Remarkably, such Sn-ene QDs with plentiful highly-active sites afford a superior CO<sub>2</sub>RR activity, delivering the industry-compatible current densities up to 1000 mA cm<sup>-2</sup> with near-unity selectivity for formate production in a flow cell, and are ultrastable to continuously operate in a wide pH range. The operando ATR-IR spectroscopy and theoretical calculations further deciphered that the rich edge centers of Sn-ene QDs hold a much higher reactivity and the residual cyano ligands with electron-withdrawing nature coordinated to the Sn atoms favor the stabilization of the CO<sub>2</sub>RR intermediate. This work could provide a bright prospect of the metallene QDs as a new paradigm for heterogeneous catalysis.

## Introduction

Electrochemical CO<sub>2</sub> reduction reaction (CO<sub>2</sub>RR) toward value-added chemicals and fuels is an important transformation route with high application prospect, due to its environment-friendly nature and compatibility with other renewable energy sources [1–6]. However, the more kinetically preferred H<sub>2</sub> evolution reaction (HER) always outperforms the CO<sub>2</sub>RR in aqueous solution, thus decreasing the selectivity of target products. Therefore, the development of the electrocatalysts with high catalytic selectivity (Faraday efficiency (FE)), activity (current density) and stability is essential to implement this technology. Due to the relatively weaker binding energy of the intermediates of CO<sub>2</sub> reduction compared to that of H\* derived from HER, CO<sub>2</sub> conversion over some specific metal-based electrocatalysts is considered a promising approach. Various metallic electrocatalysts, such as Au [7–10], Ag [11, 12], Pd [13–15], Bi [16, 17] have exhibited high selectivity for producing carbon monoxide, as well as formate, while Cu [18–28] prefers producing multiple hydrocarbons.

Due to the open double-sided surfaces possessing abundant exposed surface atoms, two-dimensional (2D) materials have recently attracted considerable attention, which not only facilitates the escape of surface atoms from the lattice to form surface defects but also makes their atomic structures easy to modify by various strategies [29–31]. In the large family of 2D materials, metallenes, the newly emerging 2D metallic materials of atomic thickness, have been regarded as ascendant CO<sub>2</sub>RR electrocatalysts owing to their multiple structural merits, such as hcp Co nanosheets (NSs) [32], n-Cu NSs [33], Tri-Ag nanoplates [34], Pd NSs [35, 36], Sb NSs [37], and bismuthene (Bi-ene) [38–41]. Compared to their bulk counterparts, the superior catalytic performance mainly originates from their plentiful facet sites and low-coordinated edge sites. Particularly, unlike the facet atoms, these atoms on the edges generally are in a highly asymmetric environment with lower coordination numbers, which could lead to a distinguished property for catalysis. In addition, the heterogeneous electron transfer rate on the edge is observed to be obviously faster than that on the plane [42].

Further reducing the lateral sizes of 2D materials down to less than 10 nm allows for preparing a new class of nanostructures, namely, quantum dots (QDs), which can not only inherit the intriguing properties of the maternal 2D materials, but also exhibit the unique quantum size effects, e.g., modified charge distribution [43–45]. In the 2D QDs, the structural defects involving the lower-coordination plane edge atoms occupy a large portion of the total atoms, inducing distinctive physicochemical/electronic properties and additional advantages for electrocatalytic applications. For example, Gopalakrishnan et al. prepared a hetero-dimensional nanostructure consisting of MoS<sub>2</sub> QDs decorated MoS<sub>2</sub> NSs, which exhibits high electrocatalytic HER activity mainly ascribed to the largely exposed active edge sites of MoS<sub>2</sub> [46]. Besides, Zhao et al. synthesized a heterophase 1T/2H WS<sub>2</sub> QDs for HER application, in which the reduced size and the improved conductivity from the metallic phase endow the WS<sub>2</sub> QDs with an excellent HER activity [47]. Similarly, it has also been reported that the edge defects on the metallene layers could display higher intrinsic activity as compared to the facet atoms [48]. Thus, it can be concluded that for 2D electrocatalytic materials, reducing their lateral size could be equally important for the performance improvement. Nevertheless, the study on metallene QDs for electrocatalysis has not been reported to date, which may be due to its great challenge in the controllable synthesis.

Moreover, the decoration of metal surface with functional additives has been reported to be an efficient strategy to tune the electronic structures of the active centers and their adsorption energy and thus boost the intrinsic catalytic properties for CO<sub>2</sub>RR. For example, Cho et al. reported that the CN and Cl adsorbed Au electrodes show a lower onset potential and exhibit around 80% CO selectivity at –0.39 V while bare Au shows below 20% selectivity [49]. They suggested that the improvement of CO selectivity is originated from van

der Waals interactions of the key reaction intermediates with these anionic species. Additionally, thiocyanate-modified Ag nanofoam could modify the local electron density of the active sites and promote the formation of COOH\* intermediates [50]. Consequently, we anticipate that the preparation of tiny atomic-thin metallene QDs with high density of the edge sites and the decoration of functional groups will be certainly a promising approach for developing high-quality electrode materials for CO<sub>2</sub>RR.

Herein, for the first time, we report the synthesis of the few-atom-layer stanene QDs (Sn-ene QDs) as a new paradigm for high-performance electrocatalysis. The Sn-ene QDs with the lateral size of ~ 8.0 nm and the thickness of ~ 1.0 nm were readily self-reconstructed from the monolayer SnFe-based Prussian blue analogue nanosheets (SnFe-PBA-NSs), which can be synthesized on a large scale (up to 158.3 grams in one batch) using a facile ultrasonic-assisted self-assembly method combined with a fluid-flow control system. These tiny Sn-ene QDs are seized of the abundance of exposed active sites, particularly the edge centers, and thus promise great room for significantly elevating the electrocatalytic activity. As a result, the derived Sn-ene QDs as a highly active electrocatalyst can accomplish an unparalleled CO<sub>2</sub>RR performance with industry-compatible current densities up to 1000 mA cm<sup>-2</sup> and near-unity selectivity for CO<sub>2</sub> electroreduction toward formate production in a flow cell. Meanwhile, it is also ultrastable to steadily operate in the wide ranges of current density and pH value. The density functional theory (DFT) calculations and operando attenuated total reflection-infrared (ATR-IR) spectroscopy unraveled that the rich edge centers of Sn-ene QDs present a much higher reactivity and the residual cyano ligands with the electron-withdrawing character coordinated to the Sn atoms is beneficial for the stabilization of the CO<sub>2</sub>RR intermediate.

## Results

### Synthesis and characterization of SnFe-PBA-NSs and Sn-ene QDs

The monolayer NSs of SnFe-PBA with molecular formula Sn<sub>a</sub>[Fe(CN)<sub>6</sub>]<sub>b</sub>·nH<sub>2</sub>O were prepared by using a facile ultrasonic-assisted self-assembly method combined with a fluid-flow control system at ambient temperature without any additive or template (Fig. 1a and Supplementary Fig. 1). Briefly, the solutions of SnCl<sub>2</sub>·2H<sub>2</sub>O and K<sub>3</sub>[Fe(CN)<sub>6</sub>] were simultaneously and continuously added into the distilled water using a fluid-flow control system under ultrasonic irradiation, which could result in the rapid reaction between Sn<sup>2+</sup> and [Fe(CN)<sub>6</sub>]<sup>3-</sup> and thus the ultrathin thickness of the generated SnFe-PBA. After aging for improving the crystallinity degree of SnFe-PBA-NSs, the as-prepared product was obtained by filtration and vacuum freeze-drying with a high output up to 158.3 g in one batch. Owing to the multiple merits (e.g., simple operation, easy automation and reliability) of this synthetic strategy, the amplified production of SnFe-PBA-NSs can be readily achieved, which is of importance for its practical implementation. Subsequently, the SnFe-PBA-NSs underwent the electrochemical self-reconstruction and transformed into the few-atom-layer Sn-ene QDs with thin thickness and rich edge centers, which can be employed as a high-performance electrocatalyst for electrochemical CO<sub>2</sub>RR (Fig. 1b).

The structure and morphology of the resultant SnFe-PBA-NSs were analyzed by diverse characterization techniques. As shown in Fig. 2a, all the diffraction peaks in the powder X-ray diffraction (PXRD) pattern of SnFe-PBA-NSs are consistent with the rhombohedral phase of Sn<sub>2</sub>[Fe(CN)<sub>6</sub>] (JCPDS no: 51-1778), which is a unique compound with layered structure according to the crystalline structure (Supplementary Fig. 3). It is remarkable that the specific surface area of SnFe-PBA-NSs reaches 105.36 m<sup>2</sup> g<sup>-1</sup> (Fig. 2b). Their morphology characterized by scanning electron microscopy (SEM) shows that the SnFe-PBA-NSs are in the form of multiple interconnected ultrathin NSs with the micron-grade lateral diameter (Fig. 2c and Supplementary Fig. 2). The average of these NSs was measured to be around 1.36 nm by atomic force microscopy (AFM), which is in good agreement with the theoretical thickness of 13.6 Å for a single layer of Sn<sub>2</sub>[Fe(CN)<sub>6</sub>], verifying the monolayer feature of SnFe-PBA-NSs (Fig. 2d,e and Supplementary Fig. 3). To acquire the microstructure details, the SnFe-PBA-NSs were further characterized by transmission electron microscopy (TEM), high-resolution TEM (HRTEM) and high-angle annular dark-field scanning TEM (HAADF-STEM). The semitransparent TEM image further confirms their ultrathin thickness of monolayer SnFe-PBA-NSs and these NSs are intertwined (Fig. 2f). In addition, the enlarged TEM image exhibits that several layers of the NSs were closely touched (Fig. 2g). Being consistent with the PXRD result, the selected area electron diffraction (SAED) pattern recorded from an individual nanosheet shows the bright diffraction spots with the rhombohedral arrangement, confirming the rhombohedral phase of SnFe-PBA-NSs (Fig. 2h). In addition, this SAED pattern can be readily indexed as the 2D in-plane reflections with the [001] zone axis direction, indicating that the nanosheet is a single crystal with the top (001) surface. It is noted that the coordination polymer NSs are sensitive to electron beam, which induced the lattice distortion to some degree. Nevertheless, the undamaged parts disclosed by HRTEM clearly display the lattice fringes with an interplanar spacing of 0.364 nm, which could be indexed as the (110) plane of SnFe-PBA (Fig. 2i), coincident with the strongest PXRD peak. The HAADF-STEM and

corresponding EDX element mapping image of SnFe-PBA-NSs proclaim the homogeneous distribution of C, N, Fe, and Sn elements within the NSs (Fig. 2j). Moreover, the composition and surface statement of SnFe-PBA-NSs were further manifested by X-ray photoelectron (XPS), Fourier transform infrared (FT-IR), Raman, and UV-vis spectroscopies (Supplementary Fig. 4).

The monolayer SnFe-PBA-NSs as the precursor were dispersed and pasted onto a carbon paper for preparing Sn-ene QDs via cathodically electrochemical reconstruction. The electrochemical treatments of SnFe-PBA-NSs with constant voltages were firstly performed between  $-0.67$  and  $-1.37$  V for 1 hour in  $\text{CO}_2$ -saturated  $0.5$  M  $\text{KHCO}_3$  electrolyte for the cathodic activation. The evolution of the PXRD patterns exhibit that all diffraction peaks of pristine SnFe-PBA-NSs gradually disappeared upon cathodic activation with increasing reduction potential, arising the new patterns attributed to elemental Sn (Fig. 3a). Meanwhile, FT-IR spectra show that the intensity of the vibration peak attributed to the cyano group gradually decreased with the increase of the applied reduction potential (Supplementary Fig. 5). These results indicate that the electrochemical self-reconstruction of SnFe-PBA-NSs into metallic Sn should involve the deconstruction of the SnFe-PBA skeleton and the reduction of the Sn cations.

Therefore, the complete production of Sn-ene QDs was performed via the electrolysis of SnFe-PBA-NSs at  $-1.17$  V for 1 h, and their structure and composition were surveyed by various characterizations. The full transformation of SnFe-PBA-NSs was confirmed by the PXRD test (Supplementary Fig. 6), while FT-IR and XPS spectra revealed a trace of residual cyano group within the derived Sn-ene QDs (Supplementary Fig. 7), which could be bonded to the undercoordinated Sn atoms. TEM images demonstrate that the as-obtained Sn-ene QDs display a small and ultrathin nanosheet dot morphology with the average lateral size of  $\sim 8.5$  nm (Fig. 3b,d). HRTEM image clearly shows the obvious lattice fringes of Sn-ene QDs with the spacings of  $0.279$  and  $0.291$  nm (Fig. 3c and Supplementary Fig. 8), corresponding to the (200) and (101) planes of tetragonal Sn, respectively. The thickness of Sn-ene QDs was analyzed to be  $\sim 1.0$  nm according to the AFM measurement (Fig. 3e and Supplementary Fig. 9), corresponding to only about 2–3 atomic layers. EDX line scanning and elemental mapping show that there is small contents of C, N and Fe remained in Sn-ene QDs and all elements are highly dispersed (Supplementary Fig. 10), which is aligned with the FT-IR and XPS results. For the electrochemical transformation, we speculated a possible mechanism for the formation of Sn-ene QDs (Fig. 3f and Supplementary Fig. 11). As the reduction potential was applied to the electrode, SnFe-PBA-NSs acted as a self-sacrificial template and the reduced zero-valence Sn atoms were grown along the nanosheet layers into Sn-ene, accompanied with the gradual breaking of Sn-N bonds, dissociation of the cyano ligands, and formation of Sn-Sn bonds (Fig. 3f), which is similar to the epitaxial Sn-ene on a surface alloy [51, 52]. However, due to corresponding large space shrinkage rate from  $\text{Sn}_2\text{Fe}(\text{CN})_6$  to metallic Sn and the gradual collapsing of the templating layers of SnFe-PBA-NSs, the growth process of the Sn-ene will be interrupted and thus form the tiny Sn-ene QDs (Supplementary Fig. 11).

## Discussion

In summary, few-atom-layer and tiny Sn-ene QDs with rich edge centers were pioneeringly fabricated via a fast electrochemical self-reconstruction from the easily-scalable monolayer SnFe-PBA-NSs, which are capable of catalyzing  $\text{CO}_2$ RR with small onset potential, large cathodic current density, high Faradaic efficiency and good stability for formate production, exceeding most of Sn-based electrocatalysts. Remarkably, the unprecedented  $\text{CO}_2$ RR performance of such unique metallene QD catalyst has been delineated with the industry-compatible ampere-level current density ( $1000 \text{ mA cm}^{-2}$ ) and extraordinary stability ( $200 \text{ mA cm}^{-2}$ , 100 h) for formate production in a wide pH range, which even outperforms those state-of-the-art electrocatalysts for  $\text{CO}_2$ RR. Additionally, operando ATR-IR spectroscopy and DFT calculations suggest that the abundant edge centers of Sn-ene QDs display superb intrinsic activity and the decoration of cyano ligand to Sn atoms further facilitates formate production by optimizing the binding of the reaction intermediate  $^*\text{OCHO}$ . This work provides the promising electrocatalytic applications of the metallene QDs as a new paradigm and promotes the industrialization prospect of the  $\text{CO}_2$ -to-formate electrosynthesis.

## Methods

### Chemicals

Tin (II) chloride dihydrate ( $\text{SnCl}_2 \cdot 2\text{H}_2\text{O}$ ), Tin (IV) chloride pentahydrate ( $\text{SnCl}_4 \cdot 5\text{H}_2\text{O}$ ), potassium ferricyanide ( $\text{K}_3[\text{Fe}(\text{CN})_6]$ ), sodium borohydride ( $\text{NaBH}_4$ ), L-cysteine ( $\text{C}_3\text{H}_7\text{NO}_2\text{S}$ ), hydrochloric acid (36 ~ 38%, HCl), potassium bicarbonate ( $\text{KHCO}_3$ ), potassium hydroxide (KOH), 1-methyl-2-pyrrolidinone (NMP), N,N-dimethylformamide (DMF), and ethanol were obtained from Sinopharm Chemical Reagent Co. Ltd. Dimethyl sulfoxide-D6 (99.9%, DMSO), deuterium oxide ( $\text{D}_2\text{O}$ ), and stannous octoate ( $\text{C}_{16}\text{H}_{30}\text{O}_4\text{Sn}$ ) was purchased from Adamas Reagent Co., Ltd. Formic acid ( $\text{HCOOH}$ ) was purchased from Energy Chemical Co., Ltd. Pluronic® F-127, and Nafion solution

(5 wt%) was obtained from Sigma-Aldrich. Graphene oxide (GO) dispersion solution (5.88 mg mL<sup>-1</sup>) was purchased from Shandong Yuhuang New Energy Technology Co., Ltd. Calcium hydroxide (98%, Ca(OH)<sub>2</sub>) was acquired from Acros Organics Co., Ltd. All chemical reagents were used directly without further purification. Ultrapure water (> 18.25 MΩ cm) was used for the experiments.

## Instrumentation

The powder X-ray diffraction (PXRD) patterns were recorded on a Miniflex600 X-ray diffractometer at 40 kV and 40 mA with Cu Kα radiation in 2θ ranging from 10° to 80°. Field emission scanning electron microscopy (FESEM) was performed on a JSM6700 microscope operated at 5 kV. Transmission electronic microscopy (TEM) and high-resolution TEM (HRTEM) equipped with energy dispersive spectrometer (EDX) were conducted on a Talos-F200X microscope operated at 200 kV. Atomic force microscopy (AFM) images were obtained on a Bruker Dimension ICON atomic force microscope. X-ray photoelectron spectroscopy (XPS) analyses were taken on Thermo Fisher Scientific XPS ESCALAB 250Xi instrument with an Al-Kα (1486.8 eV) X-ray source using C 1s (284.8 eV) as the reference. The Fourier transform infrared (FT-IR) spectra were tested on a Spectrum One Fourier transform infrared spectrometer (Perking-Elmer Instruments) by using the KBr as a background. Operando attenuated total reflection-infrared (ATR-IR) spectra were recorded on the NICOLET 6700 instrument. Raman spectra were conducted on LabRAM HR evolution with 532 nm wavelength laser source. The Brunauer-Emmett-Teller (BET) specific surface areas of the samples were measured with N<sub>2</sub> adsorption/desorption isotherms at liquid nitrogen temperature using automatic volumetric adsorption equipment (BELSORP Max analyzer). UV-vis diffuse reflectance spectra were collected on a Hitachi U-3010 spectrophotometer using BaSO<sub>4</sub> as a reference.

## Preparation

### Preparation of SnFe-PBA-NSs

In a typical process for preparation of monolayer SnFe-PBA-NSs, 135.38 g of SnCl<sub>2</sub>·2H<sub>2</sub>O and 65.85 g of K<sub>3</sub>[Fe(CN)<sub>6</sub>] were dissolved in 800 mL of distilled water, respectively. The two solutions were simultaneously and continuously added into 400 mL of distilled water using a fluid-flow control system under ultrasonic irradiation. After stirring and ultrasonic vibration for 60 min, the mixture was aged for 24 hours. Afterwards, the product was collected by filtration, washed several times with water, and dried by vacuum freeze-drying, and finally, 158.3 g of the white solid was obtained in one batch.

*Preparation of Sn-ene QDs:* Sn-ene QDs was obtained via an in situ electrochemical self-reconstruction process from SnFe-PBA-NSs in a three-electrode system. Typically, 10.0 mg of SnFe-PBA-NSs was dispersed in the mixture of water, ethanol and 5 wt% Nafion solution (8:1:1) with ultrasonic treatment for 30 min, and casted onto a 1.0×1.0 cm<sup>2</sup> carbon paper with the mass loading of 2.0 mg cm<sup>-2</sup>. The transformation was carried out in a H-type cell with two compartments separated by a piece of proton exchange membrane (Nafion 117). The working electrode and the reference electrode (saturated Ag/AgCl) were placed in the cathode compartment, and the counter electrode (Pt mesh) was placed in the anodic compartment. Each compartment contained 0.5 M KHCO<sub>3</sub> electrolyte (15 mL). All potentials were converted to the reversible hydrogen electrode (RHE) reference scale (ERHE = E<sub>Ag/AgCl</sub> + 0.198 V + 0.0591 V × pH). The cathodic transformation of SnFe-PBA-NSs to Sn-ene-QDs was performed via the electrolysis of SnFe-PBA-NSs at -1.17 V for 1 h in CO<sub>2</sub>-saturated 0.5 M KHCO<sub>3</sub> electrolyte, and the corresponding loading amount of Sn-ene QDs was calculated to be about 0.93 mg cm<sup>-2</sup>.

### Preparation of SnFe-PBA-NCs

SnFe-PBA-NCs were synthesized according to a previously reported work with some modifications [67]. Typically, 140 mg of SnCl<sub>4</sub>·5H<sub>2</sub>O and 100 mg of F127 were dispersed in a mixed solution containing 16 mL of distilled water, 14 mL of ethanol, and 2 mL of 0.01 M HCl. After stirring for 15 min, 6 mL of 0.089 M K<sub>3</sub>Fe(CN)<sub>6</sub> aqueous solution was added into the above solution and stirred for 15 min at 25°C. Afterward, the mixture solution was transferred into an autoclave and crystallized at 80°C for 10 h. The product was collected, washed with distilled water and ethanol, and then dried at 60°C for 8 h under vacuum.

### Preparation of Sn NPs

2.0256 g of C<sub>16</sub>H<sub>30</sub>O<sub>4</sub>Sn was dispersed into 200 mL of DMF during vigorous stirring at 25°C, and then 2 g of NaBH<sub>4</sub> was added this solution. After stirring for 4 h, the product was collected, washed with distilled water, and dried at 60°C for 8 h under vacuum.

### Preparation of SnO<sub>2</sub> NSs

2.0256 g of C<sub>16</sub>H<sub>30</sub>O<sub>4</sub>Sn was dispersed to 10 mL of DMF by ultrasound, and then the GO paper was immersed in this solution for 24 h. After adsorption, the GO paper was taken out and washed with DMF twice and dried at 150°C for 12 h in vacuum oven. Finally, the calcination of GO paper containing tin cations was performed in air sequentially at 500°C for 2 h and at 650°C for 1 h with a heating rate of 5°C min<sup>-1</sup>.

### Preparation of SnS<sub>2</sub> NSs

SnS<sub>2</sub> NSs was synthesized according to the previously reported procedure [68]. In a typical synthesis, 228 mg of SnCl<sub>2</sub>·2H<sub>2</sub>O and 349 mg of L-cysteine were dissolved in 60 mL of NMP under magnetic stirring for 3 h. Afterward, the precursor solution was solvothermally reacted at 180°C for 6 h. The product was centrifuged, washed with water and ethanol, and dried at 60°C for 12 h in vacuum oven.

## Electrochemical measurements

For CO<sub>2</sub>RR measurements, the carbon fiber paper supported Bi-ene-NW was directly used as the working electrode in the typical H-type cell with two compartments. The electrolyte was pre-saturated with Ar (pH = 8.4) or CO<sub>2</sub> (pH = 7.4). A constant CO<sub>2</sub> flow of 20 sccm was continuously bubbled into the electrolyte to maintain its saturation during CO<sub>2</sub>RR measurements. Cyclic voltammetry and polarization curves were carried out at a scan rate of 10 mV s<sup>-1</sup>.

In order to analyze the reduction products and calculate their Faradaic efficiency, the electrolysis was performed at selected potentials for 30 min. During the electrolysis, gaseous products were detected by an on-line gas chromatography (GC) (Agilent 7820A) equipped with a molecular sieve 5 Å and two porapak Q columns continuously. The concentration of H<sub>2</sub> and CO was analyzed by a thermal conductivity detector (TCD) and a flame ionization detector (FID), respectively. The quantification of gaseous products was carried out using a conversion factor derived from the standard calibration gases. The Faradaic efficiency of gaseous products was calculated as below:

$$\frac{F}{E} = \frac{N \times C \times v \times F}{V_m \times j_{\text{total}}} \times 100\%$$

1

where N is the number of electrons required to form a molecule of product, C is the measured concentration of product, v is the flow rate of CO<sub>2</sub>, F is the Faraday constant (96 480 C mol<sup>-1</sup>), V<sub>m</sub> is the molar volume of gas when temperature is 298 K, and j<sub>total</sub> is the recorded current.

Liquid products were collected at the end of each electrocatalysis and analyzed by 1H NMR (AVANCE III 400M). For the NMR, 0.5 ml of the catholyte was mixed with 0.1 ml of D<sub>2</sub>O containing dimethylsulfoxide (DMSO, 10 ppm) as the internal standard. The concentration of formate was quantitatively determined from its NMR peak area relative to that of the internal standard using the calibration curve from a series of standard formate solutions. The Faradaic efficiency of formate was calculated as follows:

$$\frac{F}{E} = \frac{n_{\text{formate}} \times Q_{\text{total}}}{Q_{\text{total}}} \times 100\%$$

2

where n<sub>formate</sub> is the measured amount of formate in the cathode compartment and Q<sub>total</sub> is total electric quantity.

Tafel slopes for formate production were calculated from the corresponding geometric current densities and the formate partial Faradaic efficiency.

The electrochemical impedance spectroscopy (EIS) was recorded at -0.73 V with the frequency ranging from 0.1 to 10<sup>5</sup> Hz at the AC amplitude of 5 mV.

The adsorption of OH<sup>-</sup> as a surrogate of CO<sub>2</sub>\*<sup>-</sup> was examined through a cathodic LSV scan between -0.4 and 0.38 V in Ar-saturated aqueous 0.1 M KOH solution at a scan rate of 10 mV s<sup>-1</sup>.

Electrochemically active surface area (ECSA) was obtained by measuring the electrochemical double-layer capacitance from the scan-rate dependence of CVs in a potential range of  $-0.18$  to  $-0.08$  V.

For ATR-IR measurements, firstly, SnFe-PBA-NSs supported on the glassy carbon electrode was electrochemically reduced into Sn-ene QDs. Then, the loaded Sn-ene QDs electrode was used as the working electrode, along with Ag/AgCl as the reference electrode, and platinum wire as the counter electrode.

### Flow cell measurements

Flow cell measurements were performed in a custom-designed flow cell reactor. It consisted of a gas diffusion electrode (GDE) loaded with SnFe-PBA-NSs ( $2.0 \text{ mg cm}^{-2}$ ,  $1.0 \times 1.0 \text{ cm}^2$ ) as the cathode, a piece of bipolar membrane as the separator, and a porous nickel foam as the anode. Ag/AgCl reference electrode was located inside the cathode compartment. During the measurements,  $\text{CO}_2$  gas was directly fed to the cathodic GDE at a rate of 20 sccm. The catholyte was 1 M  $\text{KHCO}_3$  (pH = 8.6), 1 M  $\text{K}_2\text{CO}_3$  (pH = 12.7) or 1 M KOH (pH = 14). It was forced to continuously circulate through the cathode compartment at a rate of  $40 \text{ mL min}^{-1}$ .

### Stability test

The long-term electrolysis experiment was carried out at the current density of  $200 \text{ mA cm}^{-2}$ , and the volumes of the cathodic and anodic electrolytes were fixed at 2 L. To eliminate the generation of  $\text{CO}_3^{2-}$  from the reaction of  $\text{CO}_2$  with KOH and reduce energy loss for  $\text{CO}_2\text{RR}$  in the flow cell, the enough  $\text{Ca}(\text{OH})_2$  powder was wrapped by the multilayer filter paper and placed in the cathode reservoir.

## Computational methods

Density functional theory (DFT) calculations were carried out through the Vienna ab initio simulation package (VASP) [69, 70]. The interactions between ions and electrons were described by projector augmented wave (PAW) and generalized gradient approximation (GGA) with Perdew-Burke-Ernzerhof (PBE) functional [71, 72]. The kinetic cut-off energy for the plane-wave basis set was 500 eV. The Brillouin zones were sampled with  $3 \times 3 \times 1$  Monkhorst-Pack meshes. The structures were fully relaxed until the maximum force on each atom was less than  $-0.02 \text{ eV \AA}^{-1}$  and  $10^{-5} \text{ eV}$ . To investigate the differences between edge and facet sites, we constructed the (101), (220) and (200) Sn planes with the supercell of  $3 \times 2 \times 1$ ,  $3 \times 3 \times 1$  and  $3 \times 3 \times 1$  unit cells, respectively. Where 6 atomic layers with the bottom 2 atomic layers were fixed along the y and z directions and another  $15 \text{ \AA}$  vacuum space was considered to avoid the periodic interaction along the y and z direction, respectively. When we explored the differences between Sn-ene QDs with or without adsorbed cyano group, 6 atomic layers with the bottom 2 atomic layers were fixed along the y and z directions, and the  $15 \text{ \AA}$  vacuum space was included to avoid the periodic interaction along the y and z directions, respectively.

## Data Availability

All data supporting the findings of this study are available from the corresponding author on request.

## Declarations

### Acknowledgements

The authors are grateful for the financial supports of the National Key Research and Development Program of China (2021YFA1500402), the National Natural Science Foundation of China (NSFC) (21901246, 22105203 and 22175174) and the Natural Science Foundation of Fujian Province (2020J01116 and 2021J06033).

### Author contributions

M. Z., Q. X and Q.-L. Z. conceived the research and designed the experiments. M. Z., D.-D. M., S.-g. H and X. L. carried out the synthesis, material characterizations, and electrochemical measurements. M. Z., X.-T. W. and Q.-L. Z. analyzed the data. M. Z. and W. W. designed the synthesis schematic. S. Z. worked on theoretical calculations. M. Z. and Q.-L. Z. drafted the manuscript. All authors discussed and revised the manuscript.

### Competing interests

The authors declare no competing interests.

## Additional information

Supplementary information is available for this paper at <https://doi.org/10.1038/>

## References

1. Jouny, M. *et al.* High-rate electroreduction of carbon monoxide to multi-carbon products. *Nat. Catal.* **1**, 748–755 (2018).
2. Li, C.W. *et al.* Electroreduction of carbon monoxide to liquid fuel on oxide-derived nanocrystalline copper. *Nature* **508**, 504–7 (2014).
3. Li, F. *et al.* Cooperative CO<sub>2</sub>-to-ethanol conversion via enriched intermediates at molecule–metal catalyst interfaces. *Nat. Catal.* **3**, 75–82 (2019).
4. Luc, W. *et al.* Two-dimensional copper nanosheets for electrochemical reduction of carbon monoxide to acetate. *Nat. Catal.* **2**, 423–430 (2019).
5. Wang, X. *et al.* Mechanistic reaction pathways of enhanced ethylene yields during electroreduction of CO<sub>2</sub>-CO co-feeds on Cu and Cu-tandem electrocatalysts. *Nat Nanotechnol.* **14**, 1063–1070 (2019).
6. Zhong, M. *et al.* Accelerated discovery of CO<sub>2</sub> electrocatalysts using active machine learning. *Nature* **581**, 178–183 (2020).
7. Liu, M. *et al.* Enhanced electrocatalytic CO<sub>2</sub> reduction via field-induced reagent concentration. *Nature* **537**, 382–386 (2016).
8. Saberi Safaei, T. *et al.* High-Density Nanosharp Microstructures Enable Efficient CO<sub>2</sub> Electroreduction. *Nano Lett.* **16**, 7224–7228 (2016).
9. Sun, K. *et al.* Ultrahigh Mass Activity for Carbon Dioxide Reduction Enabled by Gold-Iron Core-Shell Nanoparticles. *J. Am. Chem. Soc.* **139**, 15608–15611 (2017).
10. Zhu, W. *et al.* Active and selective conversion of CO<sub>2</sub> to CO on ultrathin Au nanowires. *J. Am. Chem. Soc.* **136**, 16132–5 (2014).
11. Kim, C. *et al.* Achieving Selective and Efficient Electrocatalytic Activity for CO<sub>2</sub> Reduction Using Immobilized Silver Nanoparticles. *J. Am. Chem. Soc.* **137**, 13844–50 (2015).
12. Lu, Q. *et al.* A selective and efficient electrocatalyst for carbon dioxide reduction. *Nat Commun.* **5**, 3242 (2014).
13. Gao, D. *et al.* Size-dependent electrocatalytic reduction of CO<sub>2</sub> over Pd nanoparticles. *J. Am. Chem. Soc.* **137**, 4288–91 (2015).
14. Han, N. *et al.* Alloyed Palladium-Silver Nanowires Enabling Ultrastable Carbon Dioxide Reduction to Formate. *Adv. Mater.* **33**, e2005821 (2021).
15. Zhou, R. *et al.* Two-Dimensional Palladium-Copper Alloy Nanodendrites for Highly Stable and Selective Electrochemical Formate Production. *Nano Lett.* **21**, 4092–4098 (2021).
16. Xia, C. *et al.* Continuous production of pure liquid fuel solutions via electrocatalytic CO<sub>2</sub> reduction using solid-electrolyte devices. *Nat. Energy* **4**, 776–785 (2019).
17. Yi, L. *et al.* Molten-Salt-Assisted Synthesis of Bismuth Nanosheets for Long-term Continuous Electrocatalytic Conversion of CO<sub>2</sub> to Formate. *Angew. Chem. Int. Ed.* **59**, 20112–20119 (2020).
18. Clark, E.L. *et al.* Electrochemical CO<sub>2</sub> Reduction over Compressively Strained CuAg Surface Alloys with Enhanced Multi-Carbon Oxygenate Selectivity. *J. Am. Chem. Soc.* **139**, 15848–15857 (2017).
19. Li, Y. *et al.* Structure-Sensitive CO<sub>2</sub> Electroreduction to Hydrocarbons on Ultrathin 5-fold Twinned Copper Nanowires. *Nano Lett.* **17**, 1312–1317 (2017).
20. Zhang, F.Y. *et al.* Cu overlayers on tetrahedral Pd nanocrystals with high-index facets for CO<sub>2</sub> electroreduction to alcohols. *Chem. Commun.* **53**, 8085–8088 (2017).
21. Niu, Z.Z. *et al.* Hierarchical Copper with Inherent Hydrophobicity Mitigates Electrode Flooding for High-Rate CO<sub>2</sub> Electroreduction to Multicarbon Products. *J. Am. Chem. Soc.* **143**, 8011–8021 (2021).
22. Peng, C. *et al.* Lithiation-Enabled High-Density Nitrogen Vacancies Electrocatalyze CO<sub>2</sub> to C<sub>2</sub> Products. *Adv. Mater.* **33**, e2103150 (2021).

23. Peng, C. *et al.* Double sulfur vacancies by lithium tuning enhance CO<sub>2</sub> electroreduction to n-propanol. *Nat. Commun.* **12**, 1580 (2021).
24. Sang, J. *et al.* A Reconstructed Cu<sub>2</sub>P<sub>2</sub>O<sub>7</sub> Catalyst for Selective CO<sub>2</sub> Electroreduction to Multicarbon Products. *Angew. Chem. Int. Ed.* **61**, e202114238 (2022).
25. Wu, Z.Z. *et al.* Identification of Cu(100)/Cu(111) Interfaces as Superior Active Sites for CO Dimerization During CO<sub>2</sub> Electroreduction. *J. Am. Chem. Soc.* **144**, 259–269 (2022).
26. Yang, B. *et al.* Accelerating CO<sub>2</sub> Electroreduction to Multicarbon Products via Synergistic Electric–Thermal Field on Copper Nanoneedles. *J. Am. Chem. Soc.* **144**, 3039–3049 (2022).
27. Yang, P.P. *et al.* Protecting Copper Oxidation State via Intermediate Confinement for Selective CO<sub>2</sub> Electroreduction to C<sub>2+</sub> Fuels. *J. Am. Chem. Soc.* **142**, 6400–6408 (2020).
28. Zhou, Y. *et al.* Spatial Confinement in Copper-Porphyrin Frameworks Enhances Carbon Dioxide Reduction to Hydrocarbons. *Cell Rep. Phys. Sci.* **1**, 100182 (2020).
29. Li, X. *et al.* Opportunity of Atomically Thin Two-Dimensional Catalysts for Promoting CO<sub>2</sub> Electroreduction. *Acc. Chem. Res.* **53**, 2964–2974 (2020).
30. Liu, H. *et al.* Recent Advances in Atomic-Level Engineering of Nanostructured Catalysts for Electrochemical CO<sub>2</sub> Reduction. *Adv. Funct. Mater.* **30**, 1910534 (2020).
31. Sun, Z. *et al.* Fundamentals and Challenges of Electrochemical CO<sub>2</sub> Reduction Using Two-Dimensional Materials. *Chem* **3**, 560–587 (2017).
32. Yin, J. *et al.* A New Hexagonal Cobalt Nanosheet Catalyst for Selective CO<sub>2</sub> Conversion to Ethanol. *J. Am. Chem. Soc.* **143**, 15335–15343 (2021).
33. Zhang, B. *et al.* Highly Electrocatalytic Ethylene Production from CO<sub>2</sub> on Nanodeficient Cu Nanosheets. *J. Am. Chem. Soc.* **142**, 13606–13613 (2020).
34. Liu, S. *et al.* Shape-Dependent Electrocatalytic Reduction of CO<sub>2</sub> to CO on Triangular Silver Nanoplates. *J. Am. Chem. Soc.* **139**, 2160–2163 (2017).
35. Zhao, Y. *et al.* Surface Reconstruction of Ultrathin Palladium Nanosheets during Electrocatalytic CO<sub>2</sub> Reduction. *Angew. Chem. Int. Ed.* **59**, 21493–21498 (2020).
36. Zhu W. *et al.* Low-coordinated edge sites on ultrathin palladium nanosheets boost carbon dioxide electroreduction performance. *Angew. Chem. Int. Ed.* **130**, 11718–11722 (2018).
37. Li, F. *et al.* Unlocking the Electrocatalytic Activity of Antimony for CO<sub>2</sub> Reduction by Two-Dimensional Engineering of the Bulk Material. *Angew. Chem. Int. Ed.* **56**, 14718–14722 (2017).
38. Yang, F. *et al.* Bismuthene for highly efficient carbon dioxide electroreduction reaction. *Nat. Commun.* **11**, 1088 (2020).
39. Zhang, M. *et al.* Engineering a conductive network of atomically thin bismuthene with rich defects enables CO<sub>2</sub> reduction to formate with industry-compatible current densities and stability. *Energy Environ. Sci.* **14**, 4998–5008 (2021).
40. Fan, J. *et al.* Large-Area Vertically Aligned Bismuthene Nanosheet Arrays from Galvanic Replacement Reaction for Efficient Electrochemical CO<sub>2</sub> Conversion. *Adv. Mater.* **33**, e2100910 (2021).
41. Cao, C. *et al.* Divergent Paths, Same Goal: A Pair-Electrosynthesis Tactic for Cost-Efficient and Exclusive Formate Production by Metal–Organic-Framework-Derived 2D Electrocatalysts. *Adv. Mater.* **33**, 2008631 (2021).
42. Tan, S.M. *et al.* Pristine Basal-and Edge-Plane-Oriented Molybdenite MoS<sub>2</sub> Exhibiting Highly Anisotropic Properties. *Chem. Eur. J.* **21**, 7170–8 (2015).
43. Xu, Y. *et al.* Recent progress in two-dimensional inorganic quantum dots. *Chem. Soc. Rev.* **47**, 586–625 (2018).
44. Zhai, W. *et al.* Nanodots Derived from Layered Materials: Synthesis and Applications. *Adv. Mater.* **33**, e2006661 (2021).
45. Zhang, X. *et al.* Recent Progress in the Preparation, Assembly, Transformation, and Applications of Layer-Structured Nanodisks beyond Graphene. *Adv. Mater.* **29**, 1701704 (2017).
46. Gopalakrishnan, D. *et al.* MoS<sub>2</sub> quantum dot-interspersed exfoliated MoS<sub>2</sub> nanosheets. *ACS Nano* **8**, 5297–5303 (2014).
47. Zhao, X. *et al.* Enhanced Catalytic Activities of Surfactant-Assisted Exfoliated WS<sub>2</sub> Nanodots for Hydrogen Evolution. *ACS Nano* **10**, 2159–66 (2016).

48. Prabhu, P. *et al.* Metallenes as functional materials in electrocatalysis. *Chem. Soc. Rev.* **50**, 6700–6719 (2021).
49. Cho, M. *et al.* The Role of Adsorbed CN and Cl on an Au Electrode for Electrochemical CO<sub>2</sub> Reduction. *ACS Catal.* **8**, 1178–1185 (2018).
50. Wei, L. *et al.* Thiocyanate-Modified Silver Nanofoam for Efficient CO<sub>2</sub> Reduction to CO. *ACS Catal.* **10**, 1444–1453 (2019).
51. Deng, J. *et al.* Epitaxial growth of ultraflat stanene with topological band inversion. *Nat. Mater.* **17**, 1081–1086 (2018).
52. Zhu, F.F. *et al.* Epitaxial growth of two-dimensional stanene. *Nat. Mater.* **14**, 1020–5 (2015).
53. Li, F. *et al.* Towards a better Sn: Efficient electrocatalytic reduction of CO<sub>2</sub> to formate by Sn/SnS<sub>2</sub> derived from SnS<sub>2</sub> nanosheets. *Nano Energy* **31**, 270–277 (2017).
54. Li, X. *et al.* Investigation of structural evolution of SnO<sub>2</sub> nanosheets towards electrocatalytic CO<sub>2</sub> reduction. *Chem. Asian J.* **15**, 1558–1561 (2020).
55. Salehi-Khojin, A. *et al.* Nanoparticle Silver Catalysts That Show Enhanced Activity for Carbon Dioxide Electrolysis. *J. Phys. Chem. C* **117**, 1627–1632 (2013).
56. Zhang, S. *et al.* Nanostructured tin catalysts for selective electrochemical reduction of carbon dioxide to formate. *J. Am. Chem. Soc.* **136**, 1734–7 (2014).
57. Cheng, Y. *et al.* Integrated Capture and Electroreduction of Flue Gas CO<sub>2</sub> to Formate Using Amine Functionalized SnO<sub>x</sub> Nanoparticles. *ACS Energy Lett.* **6**, 3352–3358 (2021).
58. Zu, X. *et al.* Efficient and Robust Carbon Dioxide Electroreduction Enabled by Atomically Dispersed Sn<sup>δ+</sup> Sites. *Adv. Mater.* **31**, e1808135 (2019).
59. Wu, Z. *et al.* Engineering Bismuth-Tin Interface in Bimetallic Aerogel with a 3D Porous Structure for Highly Selective Electrocatalytic CO<sub>2</sub> Reduction to HCOOH. *Angew. Chem. Int. Ed.* **60**, 12554–12559 (2021).
60. Yuan, T. *et al.* Two-Dimensional Amorphous SnO<sub>x</sub> from Liquid Metal: Mass Production, Phase Transfer, and Electrocatalytic CO<sub>2</sub> Reduction toward Formic Acid. *Nano Lett.* **20**, 2916–2922 (2020).
61. Zhu, S. *et al.* CO<sub>2</sub> Electrochemical Reduction As Probed through Infrared Spectroscopy. *ACS Energy Lett.* **4**, 682–689 (2019).
62. Cao, C. *et al.* Metal-Organic Layers Leading to Atomically Thin Bismuthene for Efficient Carbon Dioxide Electroreduction to Liquid Fuel. *Angew. Chem. Int. Ed.* **59**, 15014–15020 (2020).
63. Deng, P. *et al.* Bismuth oxides with enhanced bismuth–oxygen structure for efficient electrochemical reduction of carbon dioxide to formate. *ACS Catal.* **10**, 743–750 (2019).
64. Fan, K. *et al.* Curved surface boosts electrochemical CO<sub>2</sub> reduction to formate via bismuth nanotubes in a wide potential window. *ACS Catal.* **10**, 358–364 (2019).
65. Li, T. *et al.* Electrolyte driven highly selective CO<sub>2</sub> electroreduction at low overpotentials. *ACS Catal.* **11**, 10440–10447 (2019).
66. Han, N. *et al.* Promises of Main Group Metal–Based Nanostructured Materials for Electrochemical CO<sub>2</sub> Reduction to Formate. *Adv. Energy Mater.* **10**, 1902338 (2019).
67. Yan, Y. *et al.* Porous SnO<sub>2</sub>–Fe<sub>2</sub>O<sub>3</sub> nanocubes with improved electrochemical performance for lithium ion batteries. *Dalton Trans.* **43**, 17544–17550 (2014).
68. Han, N. *et al.* Self-templated synthesis of hierarchical mesoporous SnO<sub>2</sub> nanosheets for selective CO<sub>2</sub> reduction. *J. Mater. Chem. A* **7**, 1267–1272 (2019).
69. Kresse, G. *et al.* Ab initio molecular dynamics for liquid metals. *Phys. Rev. B* **47**, 558 (1993).
70. Kresse, G. *et al.* Efficiency of ab-initio total energy calculations for metals and semiconductors using a plane-wave basis set. *Comput. Mater. Sci.* **6**, 15–50 (1996).
71. löchl, P. *et al.* Projector augmented-wave method. *Phys. Rev. B* **50**, 17953 (1994).
72. Perdew, J. *et al.* Generalized gradient approximation made simple. *Phys. Rev. Lett.* **77**, 3865 (1996).

## Figures

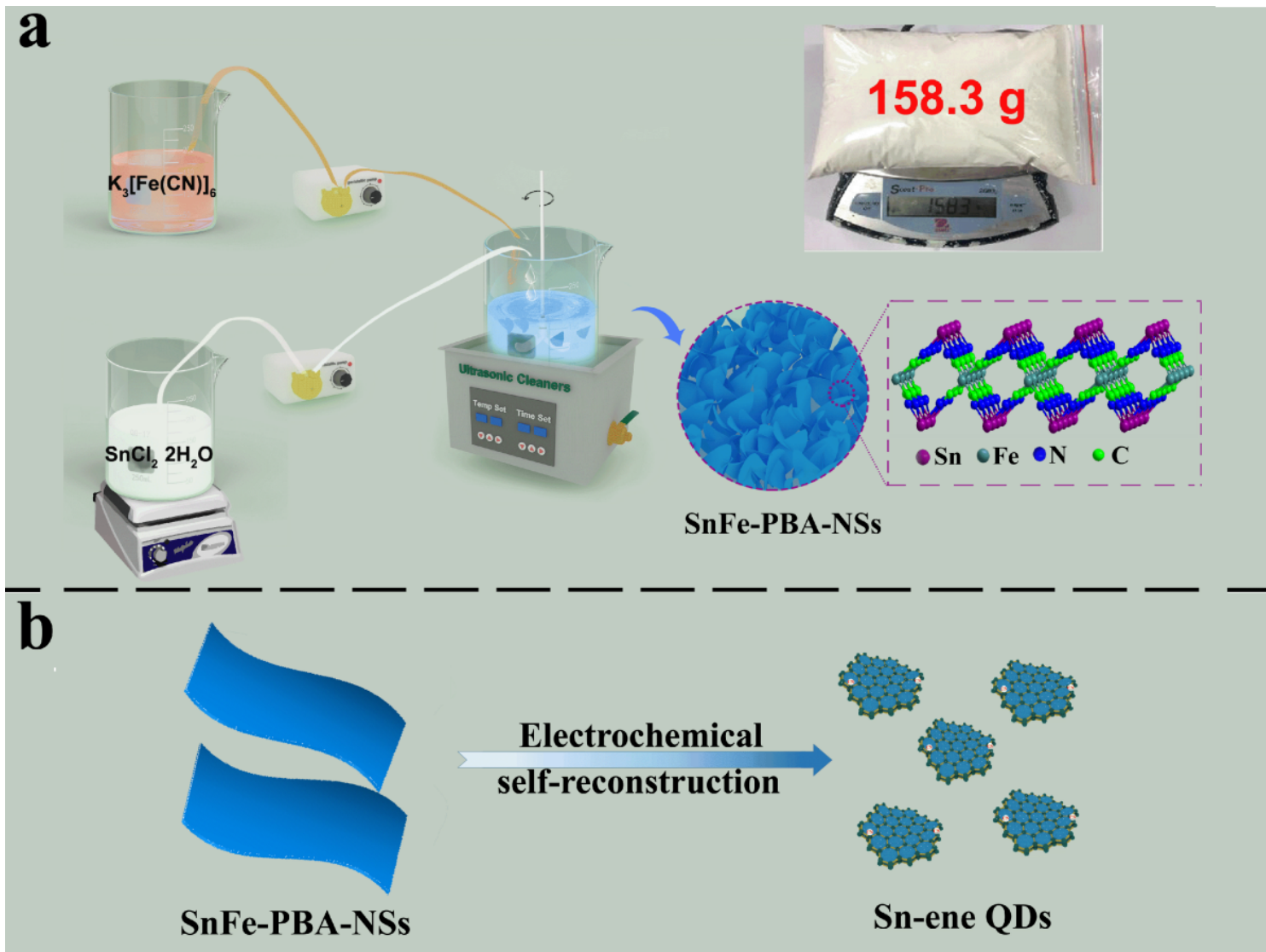
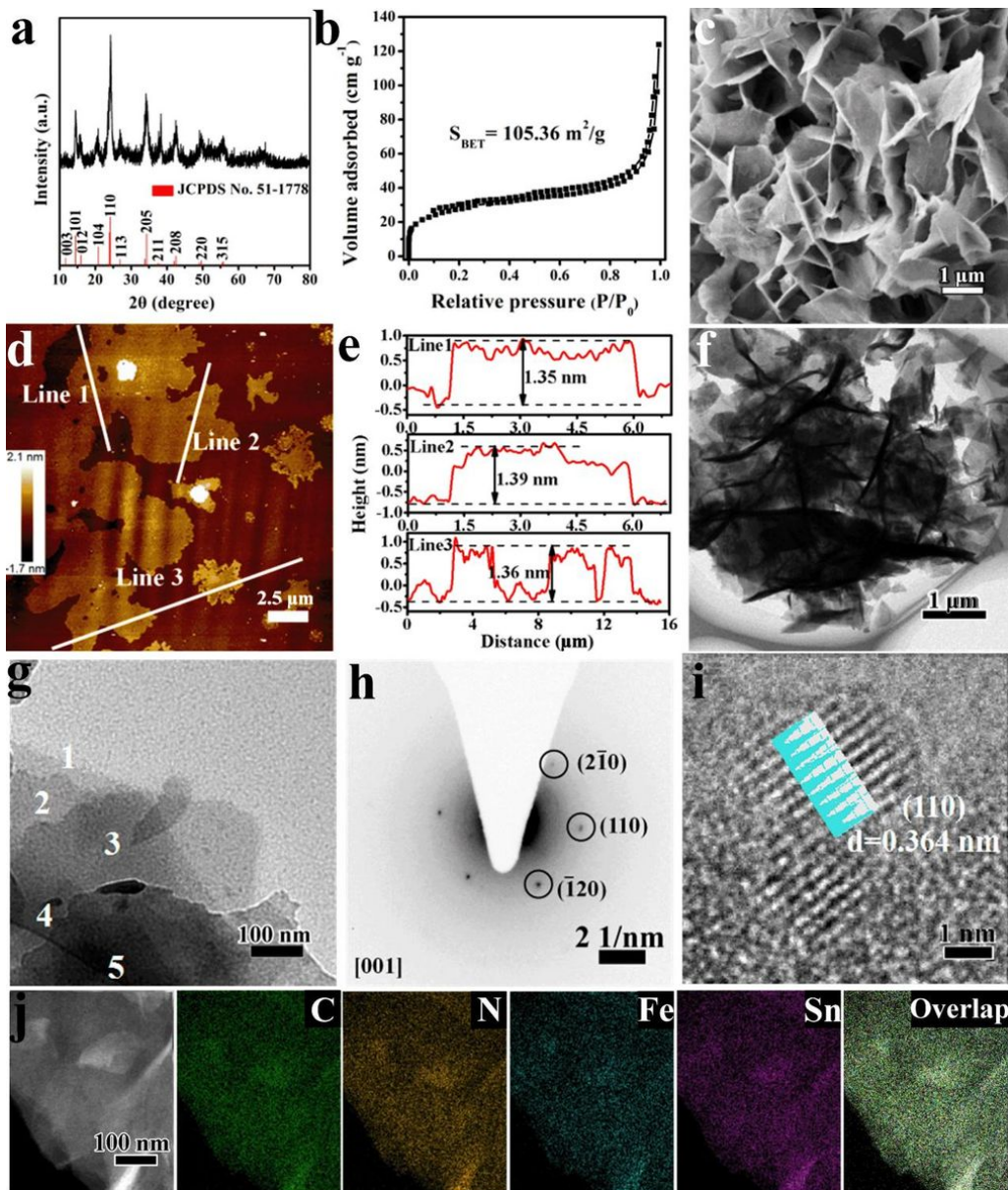


Figure 1

Preparation of Sn-ene QDs: (a) Schematic illustration of the scalable preparation of SnFe-PBA-NSs via the ultrasonic-assisted self-assembly method combined with a fluid-flow control system; (b) Schematic diagram of electrochemical self-reconstruction of SnFe-PBA-NSs to Sn-ene QDs.



**Figure 2**

Characterization of SnFe-PBA-NSs: (a) PXRD pattern; (b)  $N_2$  sorption isotherms; (c) SEM image; (d) AFM image and (e) corresponding height profiles; (f, g) TEM images; (h) SAED pattern; (i) HRTEM image; (j) HAADF-STEM and corresponding EDX element mapping images.

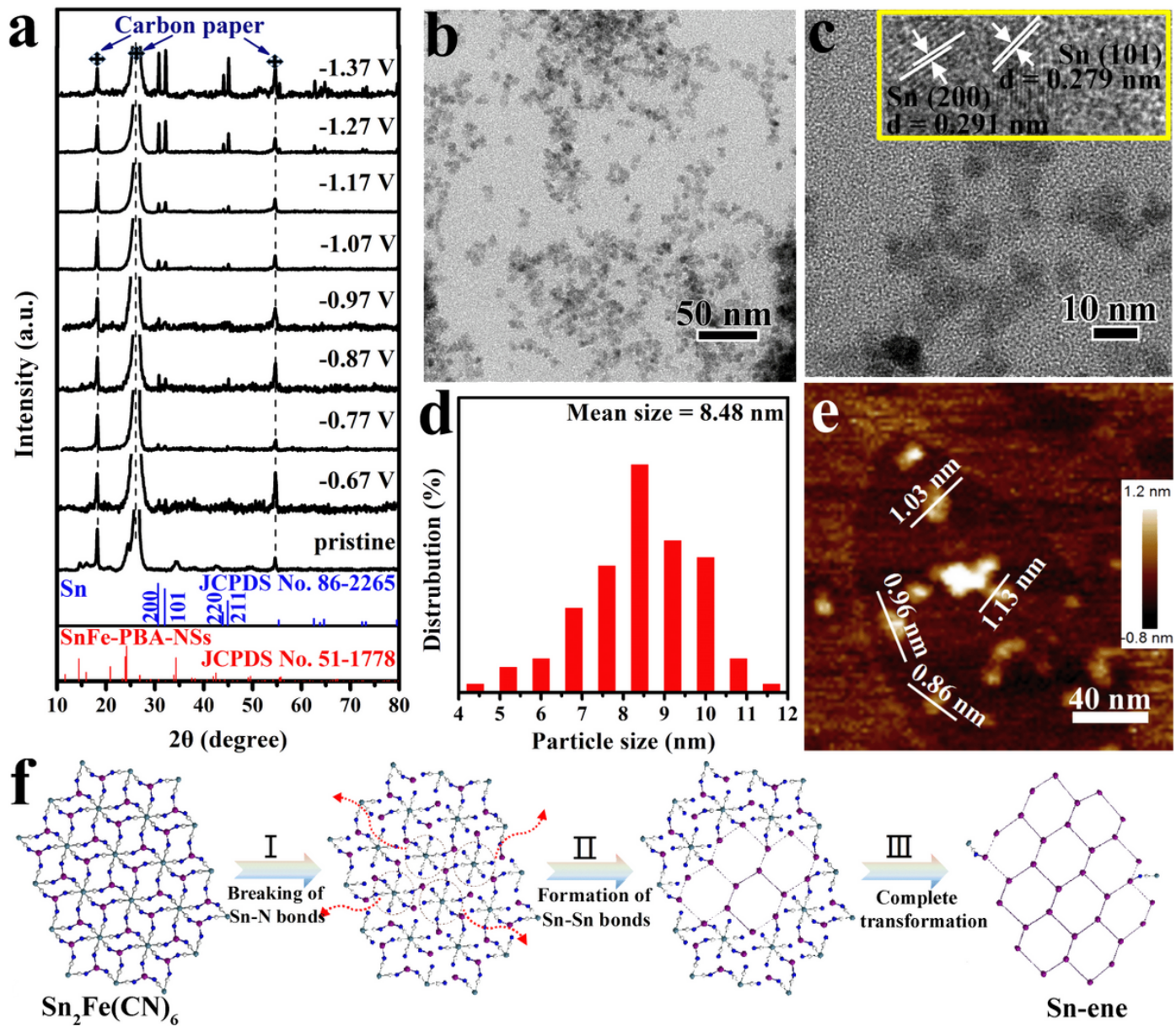
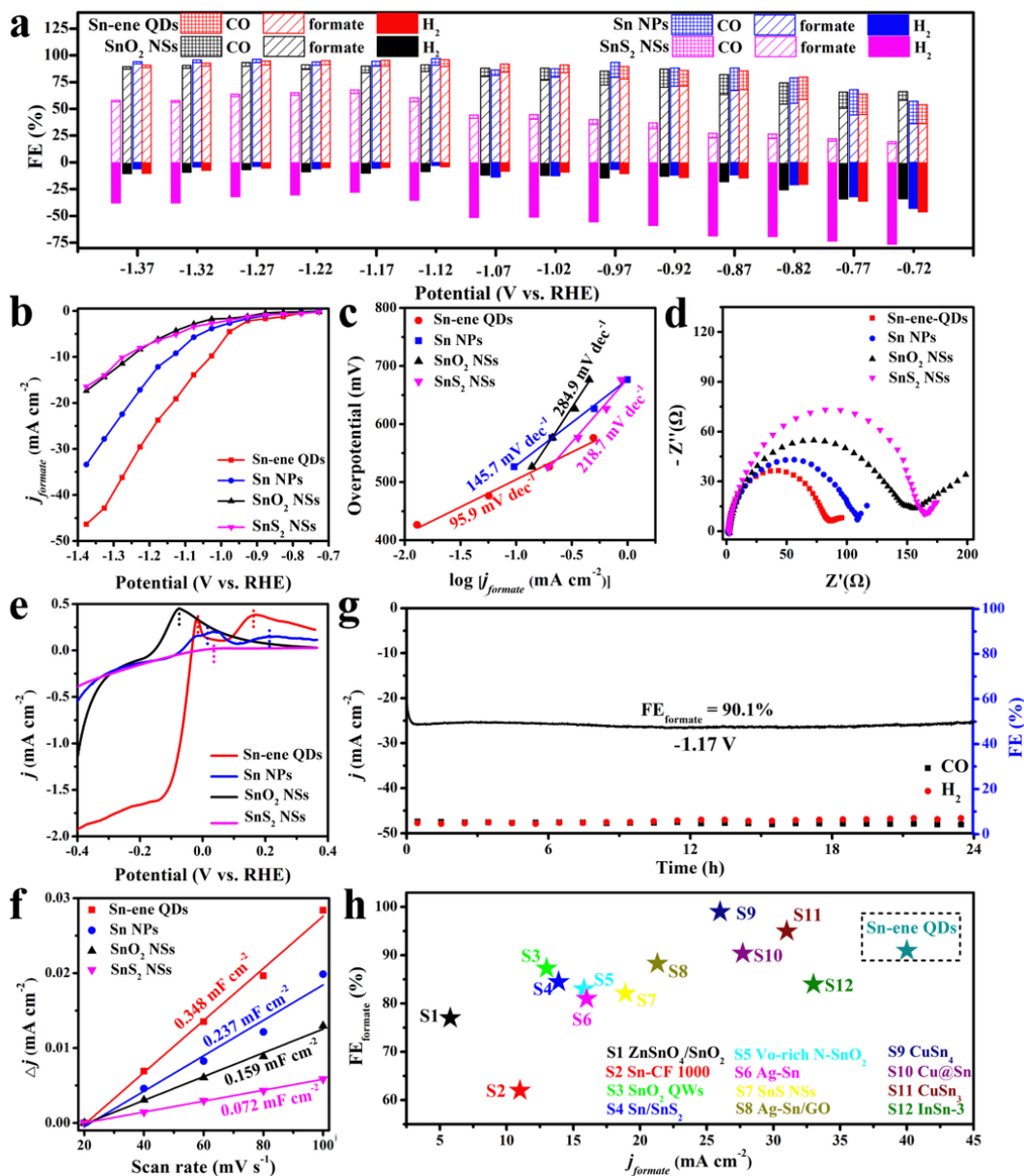


Figure 3

Structural characterizations of Sn-ene QDs: (a) evolution of PXRD patterns of Sn-ene QDs from SnFe-PBA-NSs with increasing reduction potential; (b) TEM image, (c) STEM image, (d) size distribution, (e) AFM image with the indicated thickness of Sn-ene QDs. (f) Mechanism illustration of the formation of Sn-ene QD from  $\text{Sn}_2\text{Fe}(\text{CN})_6$  template, involving the breaking of Sn-N bonds accompanied by the formation of Sn-Sn bonds.



**Figure 4**

Electrochemical CO<sub>2</sub>RR performance of Sn-ene QDs, Sn NPs, SnO<sub>2</sub> NSs, and SnS<sub>2</sub> NSs: (a) FE for formate, CO, and H<sub>2</sub> products; (b) formate partial current densities; (c) Tafel plots for CO<sub>2</sub> reduction to formate; (d) Nyquist plots obtained at -0.73 V; (e) single oxidative polarization curves in Ar-saturated 0.1 M KOH; (f) ESCAs; (g) 24 h electrolysis test for Sn-ene QDs at -1.17 V; (h) FE<sub>formate</sub> and  $j_{\text{formate}}$  comparison among a series of Sn-based catalysts and Sn-ene QDs.

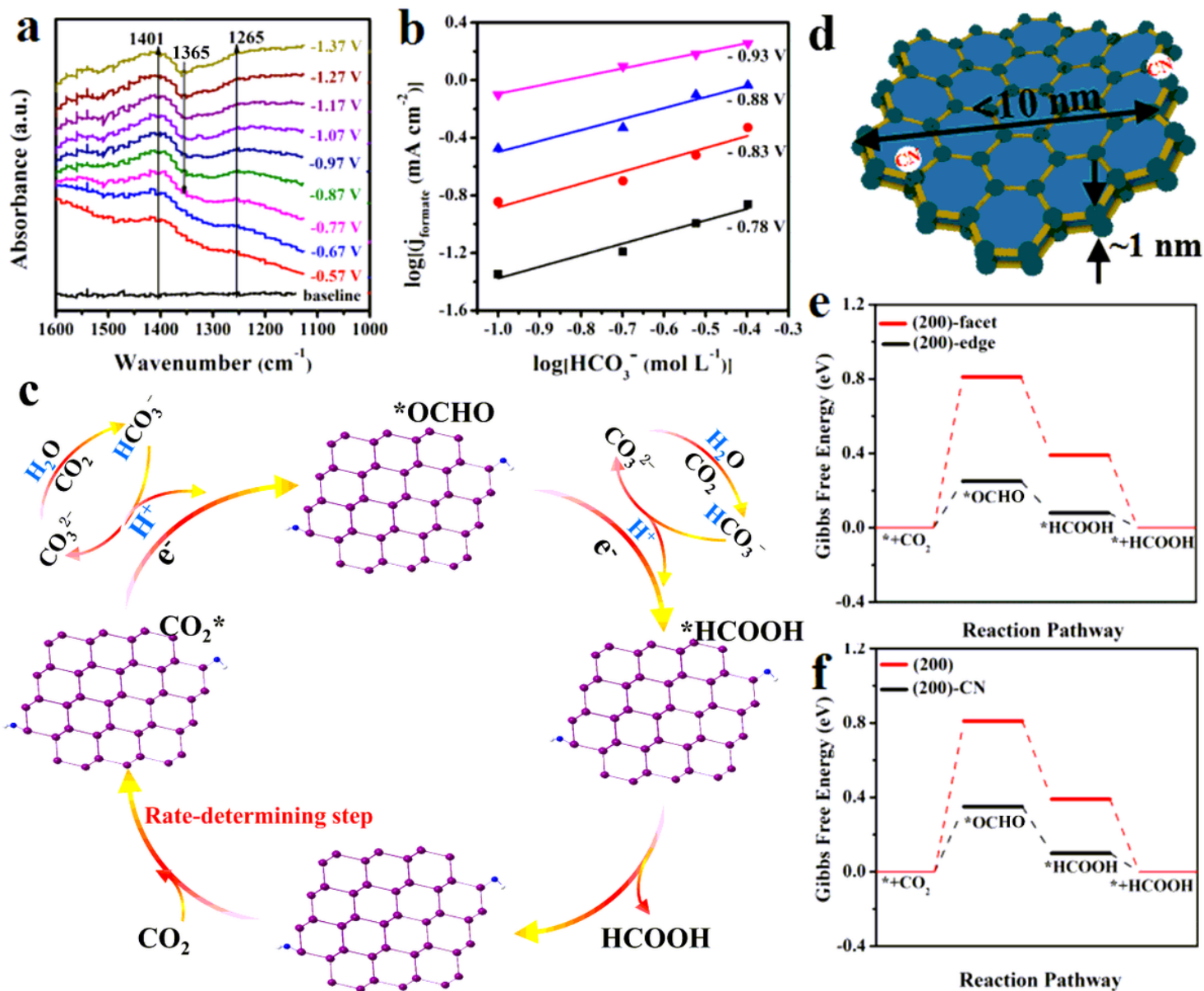


Figure 5

(a) Operando ATR-IR spectra collected in CO<sub>2</sub>-saturated 0.5 M KHCO<sub>3</sub> at different potentials over Sn-ene QDs; (b) plots of log(j<sub>formate</sub>) versus log(C<sub>HCO<sub>3</sub><sup>-</sup>) at different constant potentials in CO<sub>2</sub>-saturated 0.5 M KHCO<sub>3</sub>; (c) proposed reaction pathways for CO<sub>2</sub> electroreduction to formate on the surface of Sn-ene QDs; (d) illustration of schematic diagram of Sn-ene QDs decorated with residual cyano group; calculated free energy diagrams for CO<sub>2</sub> reduction to formate over (200) plane: (e) facet sites and edge sites, (f) facet sites with and without adsorbed cyano group.</sub>

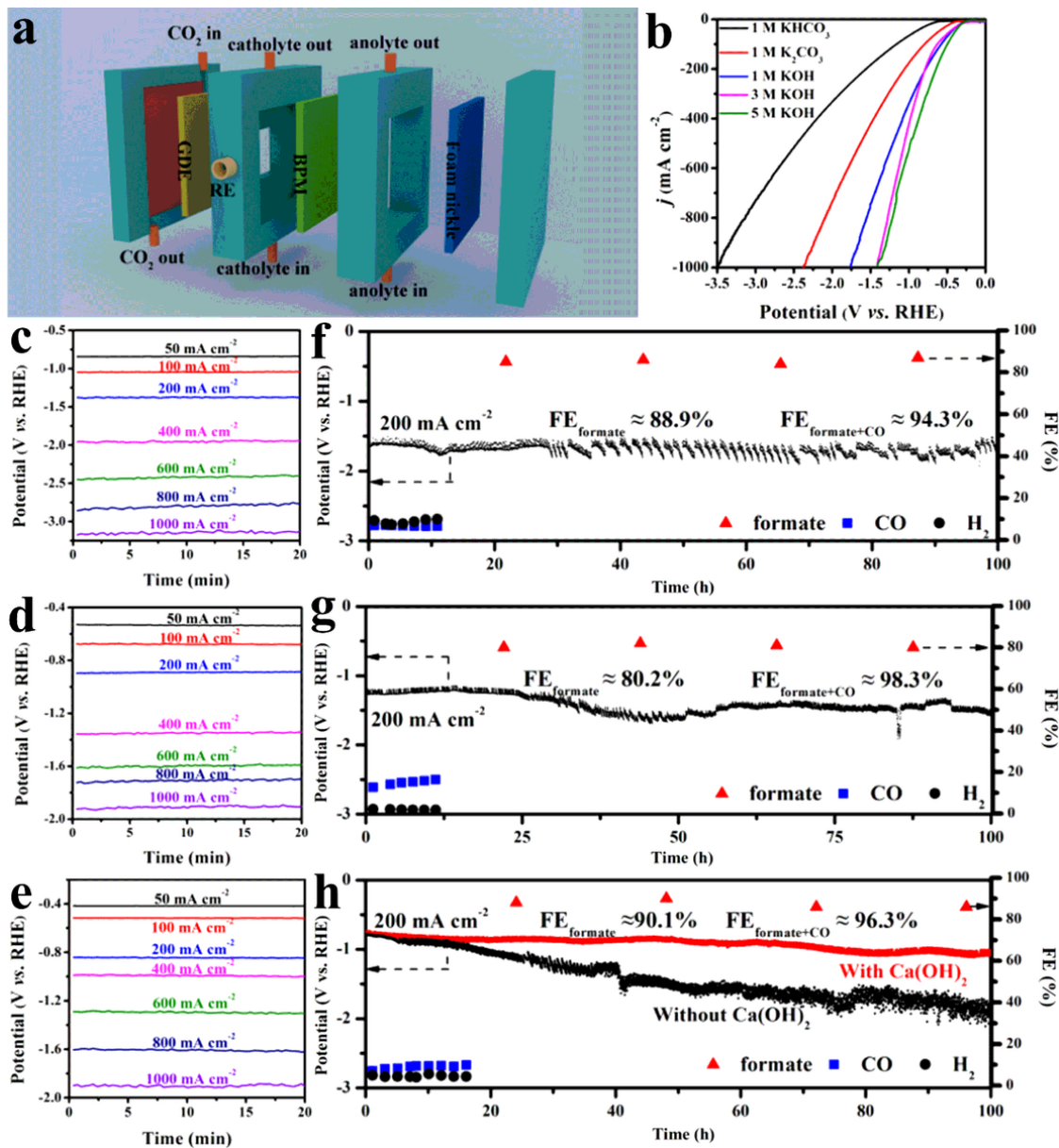


Figure 6

Electrochemical CO<sub>2</sub>RR performance of Sn-ene QDs in the flow cell: (a) schematic of the gas-fed flow cell configuration; (b) LSV curves; chronoamperometric responses at different currents in (c) 1 M KHCO<sub>3</sub>, (d) 1 M K<sub>2</sub>CO<sub>3</sub>, (e) 1 M KOH; long-term chronopotentiometric stability in (f) 1 M KHCO<sub>3</sub>, (g) 1 M K<sub>2</sub>CO<sub>3</sub>, and (h) 1 M KOH with (red line) and without (black line) addition of Ca(OH)<sub>2</sub>.

## Supplementary Files

This is a list of supplementary files associated with this preprint. Click to download.

- [Graphicalabstract.docx](#)
- [si220330.docx](#)